Shear Band Formation in Bulk Metallic Glasses

Jue Chen (University of California), **Ryan Goh** (University of Minnesota Twin Cities),
Emily McHenry (Louisiana State University), **Diego Torrejon** (George Mason University),
& **Xin Yang** (Simon Fraser University)

August 16, 2013

Abstract

In recent times, there has been a growing interest in the machining of amorphous metallic alloys, which are also called bulk metallic glasses (BMGs). These materials differ from common polycrystalline metallic alloys, because their atoms do not assemble on a crystalline lattice, and as a result, they have unique physical, mechanical, and chemical properties. A number of BMGs have been found to produce shear-localized chips during machining operations. Furthermore, a number of theoretical studies have argued that this strain localization is not controlled by rapid heating, but rather by a change in the concentration of free-volume in the material. In this work we study shear band formation in BMGs by studying a geometrically simple deformation of the material, a homogeneous shear flow. We perform a linear stability analysis of the homogeneous shear flow, obtaining a non-autonomous linear system of ODEs. Using numerical simulations of this system we show that free-volume instabilities dominate the growth of localized shear bands. Furthermore, we compare our results with simulations of the full system of PDEs. Finally, our simulations suggest that the simple shear model is not valid for long times and should only be used as an onset equation.

Contents

1   Introduction

Metallic glasses, particularly bulk metallic glasses, have become an area of particular interest in recent years because their unique physical properties are well suited for a wide array of applications in science and engineering. Metallic glasses are formed by cooling a liquid metal or alloy to its glass transition temperature fast enough to prevent the formation of the typical crystalline or polycrystalline structure of the solid. As a result, metallic glasses exhibit the amorphous structure of a liquid at a solid state, giving the material elasticity and strength. Figure 1.1 shows the structure of a polycrystalline solid compared to that of a metallic glass at the atomic level.
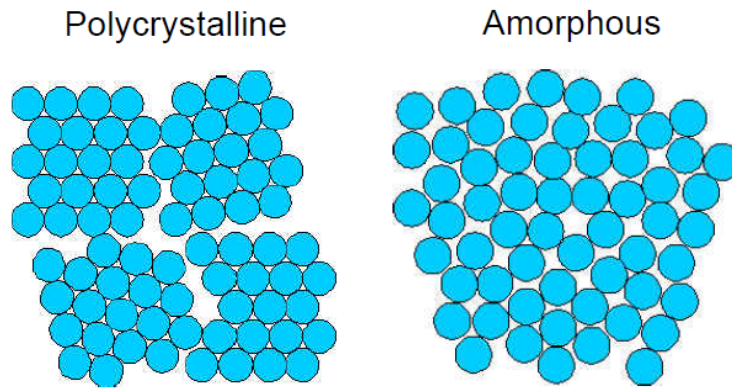

Figure 1.1: Microscopic structure of a common metal (left) versus that of a bulk metallic glass (right). From [14].

Until relatively recently, the creation of metallic glasses required very high cooling rates in order to prevent crystallization, thus limiting the quantity that could be produced at one time. However in recent decades, scientists have engineered metallic glasses, typically from alloys, that can be cooled to a glassy state more slowly. As a result, these materials, called bulk metallic glasses (BMGs), can be manufactured in large quantities.

Although the amorphous structure of BMGs causes resistance to plastic deformation, it leaves them vulnerable to catastrophic failure at high strain rates. Polycrystalline solids experience strain hardening, wherein enhanced shear at the grain boundaries is redistributed throughout the crystals,

and the solid actually strengthens as it becomes permanently deformed. At low temperatures, this leads to a relatively homogeneous deformation. Because BMGs lack a crystalline structure they cannot redistribute shear, and strain becomes localized in a very small region. Heat generated by the high shear rate causes the material to dilate and weaken, leading to lower shear resistance and an even higher shear rate. This strain softening causes the formation of extremely narrow shear bands at low temperatures, which leaves the material susceptible to fracture. Since the formation of shear bands precedes the failure of the material through fracture, it is useful to model the formation of these shear bands in order to understand the failure potential of the BMG.

In this paper, we explore the theoretical model of deformation in metallic glasses presented in [1], [4], and [3]. For a thorough review of the literature, see [6]. This paper is organized as follows, first we explore the theoretical model of deformation in metallic glasses presented in [1], [4], and [3]. Section 2 introduces the PDE model and dimensionless PDE model. In Section 3, we reconstruct the non-autonomous ODE system for perturbations of the homogeneous solutions and examine the linear stability analysis found in [3]. Section 4 explores the notion of Hadamard instability and the method of frozen coefficients to detect asymptotic stability in our model. Section 5 is devoted to the analysis of the PDE dynamics, and Section 6 contains final remarks and potential further research.

2 PDE Model for Shear Band Formation

We use a thermo-mechanical free-volume model built from the governing equations of continuum mechanics is given by

$$\rho \frac{\partial v}{\partial t} = \frac{\partial \tau}{\partial y} \tag{2.1a}$$

$$\frac{\partial \gamma}{\partial t} = \frac{\partial v}{\partial y} \tag{2.1b}$$

$$\rho C_p \frac{\partial \theta}{\partial t} = k \frac{\partial^2 \theta}{\partial y^2} + \tau \alpha_{TQ} f(\xi, \theta, \tau) \tag{2.1c}$$

$$\frac{\partial \xi}{\partial t} = \tilde{k} \frac{\partial^2 \xi}{\partial y^2} + g(\xi, \theta, \tau) \tag{2.1d}$$

$$\frac{\partial \gamma^P}{\partial t} = f(\xi, \theta, \tau) \tag{2.1e}$$

$$\frac{\partial \tau}{\partial t} = \mu \left(\frac{\partial v}{\partial y} - \frac{\partial \gamma^P}{\partial t} \right) \tag{2.1f}$$

where (2.1a) is the Cauchy momentum equation, (2.1b) is the compatibility equation, (2.1c) is the energy equation, (2.1f) is the elastic condition, and (2.1d) is the free-volume evolution equation. The parameters γ, τ, θ, ξ, and γ^P are the applied shear strain, shear stress, temperature, free-volume, and plastic shear strain, respectively. The constants ρ, C_p, k, α_{TQ}, $\tilde{k}$, and μ are, respectively, the material density, specific heat, thermal conductivity, Taylor-Quinney coefficient (fraction of plastic work converted to heat), diffusion coefficient of free-volume, and shear modulus. The constitutive laws f and g are given by,

$$f(\xi, \theta, \tau) = 2ve^{-\frac{\alpha v^*}{\xi}} e^{-\frac{\Delta G^m}{k_B \theta}} \sinh\left(\frac{\tau\Omega}{2k_B\theta}\right)$$

$$g(\xi, \theta, \tau) = v^* v e^{-\frac{\alpha v^*}{\xi}} e^{-\frac{\Delta G^m}{k_B \theta}} \left(\frac{2\alpha k_B \theta}{\xi \mu^*}\left[\cosh\left(\frac{\tau\Omega}{2k_B\theta}\right) - 1\right] - \frac{1}{n_D}\right)$$

where v is the frequency of atomic vibration, α is a geometrical factor of order 1, v^* is the hard-sphere atomic volume, ΔG^m is the activation energy, k_B is the Boltzmann constant, Ω is the atomic volume, μ^* is the effective elastic modulus, and n_D is the number of atomic jumps needed to annihilate a free-volume equal to v^*, and is usually taken to be between 3 and 10. All the parameters were obtained from [3] and are listed in appendix A.

In experiments and simulations, the strain rate has been shown to be low enough implying the irrelevance of the inertia force in the momentum equation. Such an assumption, denoted as the quasi-static approximation, has prevously been utilized by [4], [1], & [3]. As a result, the stress is uniform with respect to the space variable. We also plug equation (2.1b) into equation (2.1f), and the respective system (2.1) simplifies to

$$\rho C_p \frac{\partial \theta}{\partial t} = k\frac{\partial^2 \theta}{\partial y^2} + \tau \alpha_{TQ} f(\xi, \theta, \tau) \tag{2.2a}$$

$$\frac{\partial \xi}{\partial t} = \tilde{k}\frac{\partial^2 \xi}{\partial y^2} + g(\xi, \theta, \tau) \tag{2.2b}$$

$$\frac{\partial \gamma^P}{\partial t} = f(\xi, \theta, \tau) \tag{2.2c}$$

$$\frac{\partial \tau}{\partial t} = \mu\left(\frac{\partial \gamma}{\partial t} - \frac{\partial \gamma^P}{\partial t}\right). \tag{2.2d}$$

2.1 Dimensionless Model

We now nondimensionalize the system (2.2a)-(2.2d) in order to facilitate the ensuing stability analysis. To this end, we take $\bar{y} = y/L$, $\bar{T} = \theta/T_0$, $\bar{\tau} = \tau/\tau_0$, $\bar{\mu} = \mu/\tau_0$, $\bar{\xi} = \xi/\alpha v^*$, and $\bar{t} = t/t_0$, where $T_0 = 300K$, $\tau_0 = 2k_B T_0/\Omega$, $L^2 = kt_0/\rho C_P$, and $t_0 = v^{-1}e^{\Delta G^m/k_B T_0}$. In a slight abuse of notation, we subsequently drop the bar when referring to dimensionless parameters, and write our dimensionless model as

$$\frac{\partial \theta}{\partial t} = \frac{\partial^2 \theta}{\partial y^2} + \beta_3 \tau \frac{\partial \gamma^P}{\partial t} \tag{2.3a}$$

$$\frac{\partial \xi}{\partial t} = \beta_4 \frac{\partial^2 \xi}{\partial y^2} + g(\xi, \theta, \tau) \tag{2.3b}$$

$$\frac{\partial \gamma^P}{\partial t} = f(\xi, \theta, \tau) \tag{2.3c}$$

$$\frac{\partial \tau}{\partial t} = \mu \cdot \left(\frac{\partial \gamma}{\partial t} - \frac{\partial \gamma^P}{\partial t}\right) \tag{2.3d}$$

Where n_D, μ, μ^*, and α are dimensionless parameters and our constitutive laws take the dimensionless form given by,

$$f(\xi, \theta, \tau) = 2e^{\beta_2} e^{-\frac{1}{\xi}} e^{-\frac{\beta_2}{\theta}} \sinh\left(\frac{\tau}{\theta}\right)$$

$$g(\xi, \theta, \tau) = \frac{e^{\beta_2}}{\alpha} e^{-\frac{1}{\xi}} e^{-\frac{\beta_2}{\theta}} \left(\frac{\theta}{\beta_1 \mu^* \xi}\left[\cosh\left(\frac{\tau}{\theta}\right) - 1\right] - \frac{1}{n_D}\right).$$

3 Linear Perturbation Analysis

In this section we perform a stability analysis using the linearized form of our dimensionless system and compare it to those in the literature [3], [4], & [6]. Before doing so we outline and try to fill in the argument given in one specific, but often cited, reference [3].

If spatially homogeneous initial conditions are inserted into the dimensionless equations (2.3a) - (2.3d), the solution profiles will remain so as time evolves. We denote such solutions as $\gamma_h^P(t), \xi_h(t), \theta_h(t)$ and $\tau(t)$. Hence in this setting, the diffusion terms can be dropped, and our system can be treated as a system of ODEs. These equations can then be numerically integrated using the MATLAB ODE suite. See Figure 3.1 for plots of these solutions. We assume that the applied strain rate is constant so that the total strain $\gamma = \dot{\gamma}_0 t$ is linear in time, and thus can be treated as a scaled time variable. We shall use the two interchangeably. Also, as it will be useful in the remainder of our discussion, we denote $\gamma_M = \dot{\gamma}_0 t_M$ to be the strain at which τ attains its maximum and initiates the onset of instability.
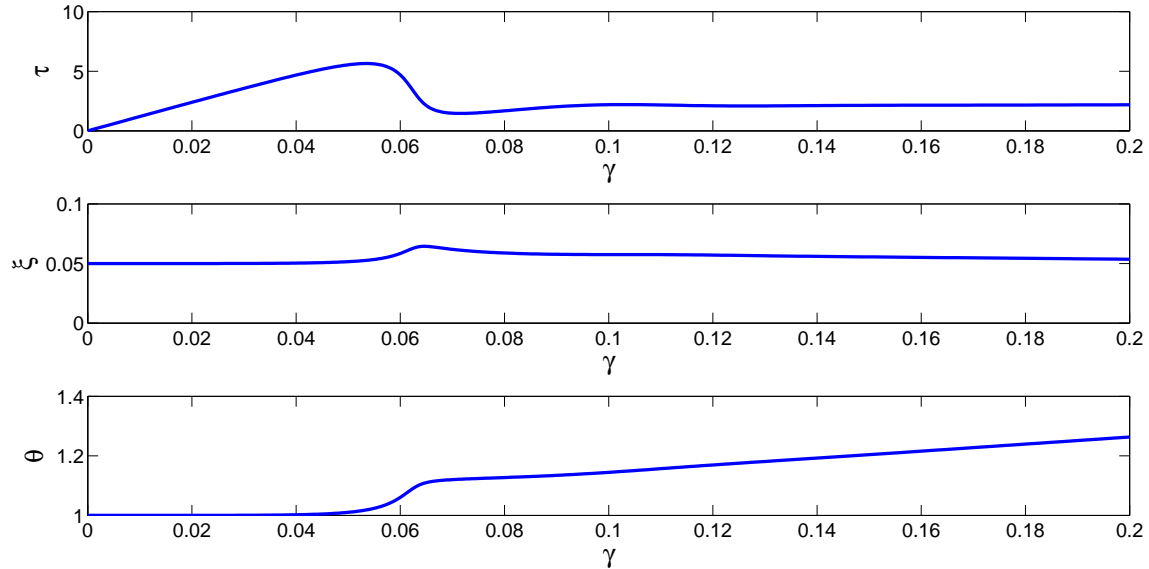

Figure 3.1: Homogeneous solutions with $\dot{\gamma}_0 t = 2 \cdot 10^{-4}$ and $t_0 = 1 \cdot 10^{-5}$. The maximum in the stress strain peak occurs at $\gamma_M \sim 0.0535$.

To leading order, the insertion of the perturbed solution

$$\gamma = \gamma_h(t) + \delta_\gamma(t)\mathrm{e}^{\mathrm{i}\omega x} \tag{3.1}$$

$$\xi = \xi_h(t) + \delta_\xi(t)\mathrm{e}^{\mathrm{i}\omega x} \tag{3.2}$$

$$\theta = \theta_h(t) + \delta_\theta(t)\mathrm{e}^{\mathrm{i}\omega x} \tag{3.3}$$

$$\tag{3.4}$$

into the dimensionless model yields the following non-autonomous linear system of ODEs

$$\frac{\partial \delta_\gamma}{\partial t} = \frac{\partial f}{\partial \xi}\delta_\xi + \frac{\partial f}{\partial \theta}\delta_\theta$$

$$\frac{\partial \delta_\xi}{\partial t} = \left(\frac{\partial g}{\partial \xi} - \beta_4(L\omega)^2\right)\delta_\xi + \frac{\partial g}{\partial \theta}\delta_\theta$$

$$\frac{\partial \delta_\theta}{\partial t} = -(L\omega)^2\delta_\theta + \beta_3\tau\left(\frac{\partial f}{\partial \xi}\delta_\xi + \frac{\partial f}{\partial \theta}\delta_\theta\right).$$

In matrix form we write this system as

$$\dot{\delta} = A(t)\delta \tag{3.5}$$

where $A(t) : \mathbb{R} \to \mathbb{R}^{3\times3}$, $\delta = (\delta_\gamma, \delta_\xi, \delta_\theta)^T$ and

$$A(t) = \begin{pmatrix} 0 & \frac{\partial f}{\partial \xi} & \frac{\partial f}{\partial \theta} \\ 0 & \frac{\partial g}{\partial \xi} - (L\omega)^2 & \frac{\partial g}{\partial \theta} \\ 0 & \beta_3\tau\frac{\partial f}{\partial \xi} & \tilde{\iota}(t) \end{pmatrix}. \tag{3.6}$$

Here

$$\tilde{\iota}(t) = \iota(t) - \tilde{\omega}^2 \tag{3.7}$$

with

$$\iota(t) = \beta_3\tau\frac{\partial f}{\partial \theta}, \qquad \text{and} \quad \tilde{\omega} = L\omega.$$

Recall that the partial derivatives are all time-dependent. For example $\frac{\partial f}{\partial \theta} = \frac{\partial f}{\partial \theta}(\xi_h(t), \theta_h(t), \tau(t))$. Here we have made the quasi-static approximation so that the momentum equation is reduced to $\tau = \tau(t)$.

3.1 Main Argument of [3]

We now wish to summarize and elucidate the thermal instability argument given in [3]. The authors argue that for parameter regimes near the peak of the stress-strain curve the terms $\frac{\partial f}{\partial \xi}$, $\frac{\partial f}{\partial \theta}$, and $\frac{\partial g}{\partial \xi}$ are positive functions of t. Thus for a small initial perturbation, δ_0, whose components are all positive, the term $\frac{d\delta_\gamma}{dt}$ will be positive for all $t > 0$. Given some trajectory $\delta(t)$ with initial condition $\delta(0) = \delta_0$, this implies that the first component of $\delta(t)$ will grow. Next [3] argues that since the equations for δ_ξ and δ_θ are linearly coupled, the dynamics of the former are determined by those of the latter.
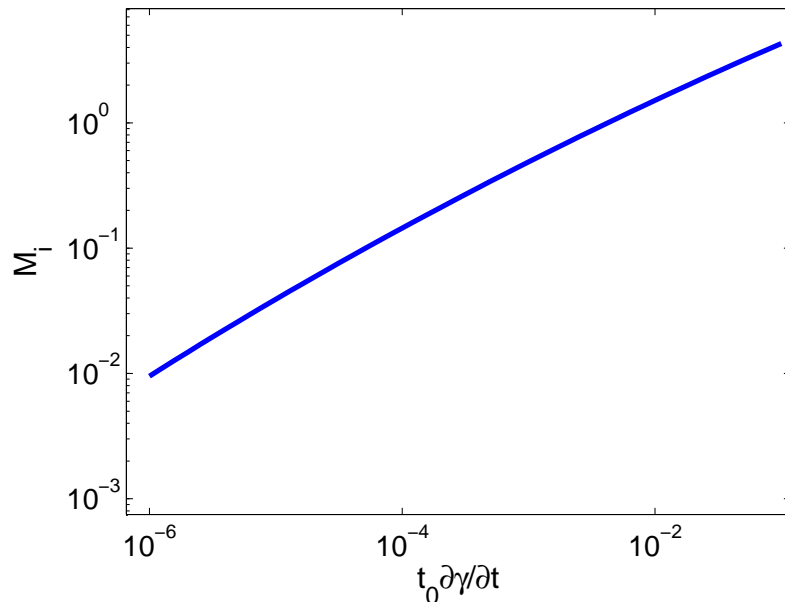
6

Figure 3.2: Instability curve given in [3].

Now since $\frac{\partial f}{\partial \xi} > 0$, they argue if

$$\tilde{\omega} < M_i := \sqrt{\max_{t \in \mathbb{R}^+} \iota(t)}. \tag{3.8}$$

there exists some finite interval I_u on which $\frac{d\delta_\theta}{dt} > 0$, implying that $\delta_\theta(t)$ must grow in this interval. They then use this fact to conclude that any initial perturbation in the first octant will grow during this time interval. Since the linear perturbation analysis is only looking at small time scales they then conclude any wave numbers $\tilde{\omega}$ satisfying this condition are unstable. The curve $M_i(\dot{\gamma}_0)$ is given in Fig 3 of [3] and is reproduced in Figure 3.2.

Though in the text of [3] the authors state that this curve gives only a necessary condition for instability, it is noted in their Fig. 3 that wave numbers $\tilde{\omega} > M_i(\gamma)$ are stable. Furthermore, they arrive at physical implications from this line of reasoning. Because of this we comment on their analysis in the following section.

3.2 Analysis of ODE Dynamics

In the following, we numerically solve the perturbation equations (3.1) - (3.3) alongside the homogenous equations and compare our results with the arguments given immediately above. As the equations are linear, solutions scale linearly with the scaling of initial conditions. Hence we choose $\delta_0 = (0, 1, 1)^T$ so that free-volume and temperature are perturbed. The solutions profiles can be found in Figure 3.3 for wave numbers above and below the stability line $M_i(\dot{\gamma})$, plotted alongside the homogeneous solution of the stress-strain curve of the dimensionless model (2.3). Since the applied strain rate is assumed to be constant, $\gamma = t \cdot \dot{\gamma}_0$, we plot against the total strain γ.

(a) $\dot{\gamma}_0 t = 2 \cdot 10^{-6}$, $\tilde{\omega} = 0.1$, and $t_0 = 1 \cdot 10^{-5}$.

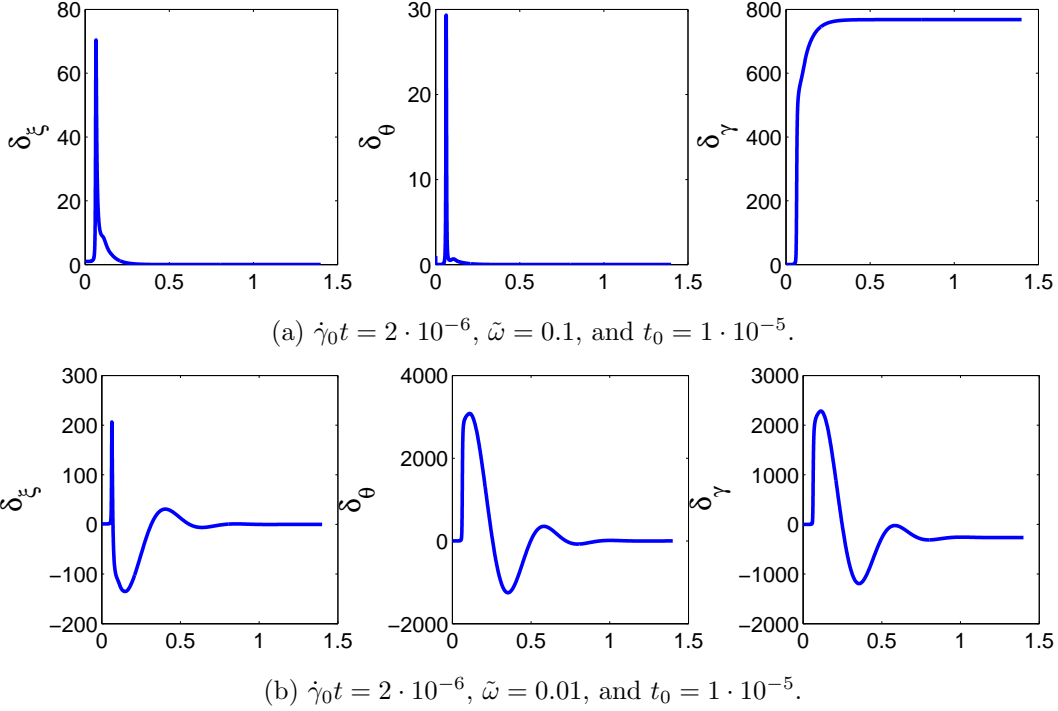(b) $\dot{\gamma}_0 t = 2 \cdot 10^{-6}$, $\tilde{\omega} = 0.01$, and $t_0 = 1 \cdot 10^{-5}$.

Figure 3.3: Solutions of the perturbed equations for (a) $\tilde{\omega} > M_i$ and $\tilde{\omega} < M_i$.

Note that the perturbations obtain their maximum as γ reaches the peak of the stress-strain curve at γ_M, and then begin to decay as γ goes past the first minimum of $\tau(\gamma)$. Since shear band localization is a transient behavior, for the moment we only focus on the dynamics leading up to the first peak in the solution profile.

As described in the previous section, reference [3] characterizes a perturbation as unstable if δ_θ grows as γ increases past γ_M, the stress-strain peak time. Observe from Figure 3.3 that both δ_θ and δ_ξ grow for values of $\tilde{\omega}$ both above and below the instability curve M_i. This suggests that the instability index $M_i(\dot{\gamma}_0)$ does not delineate a bifurcation.

Figure 3.4 gives the values of $C_\theta := \max_{t \geq 0} \delta_\theta(t)$ and $C_\xi := \max_{t \geq 0} \delta_\xi(t)$ for a range of $\tilde{\omega}$ values. The value of C_θ decreases as the wavenumber increases, while C_ξ is approximately constant before decaying for large wavenumbers.

Since β_4 is very small, the term $-\beta_4(\omega L)^2$ has very little affect on δ_ξ until $\tilde{\omega}$ is correspondingly large. As we have scaled wavenumber with the thermal length scale, localized shear bands, which have a much smaller wavelength, will have large scaled wavenumber $\tilde{\omega}$. Therefore, in accordance with [4], [6], and [10], we conclude from this figure that free-volume instabilities govern the growth of a perturbation. In other words, to study the linear stability of a perturbation, one must analyze the growth or decay of perturbations in free-volume. This was also observed in the numerical solution of the full dimensionless system of PDEs, where perturbations in free-volume dominated those in temperature.
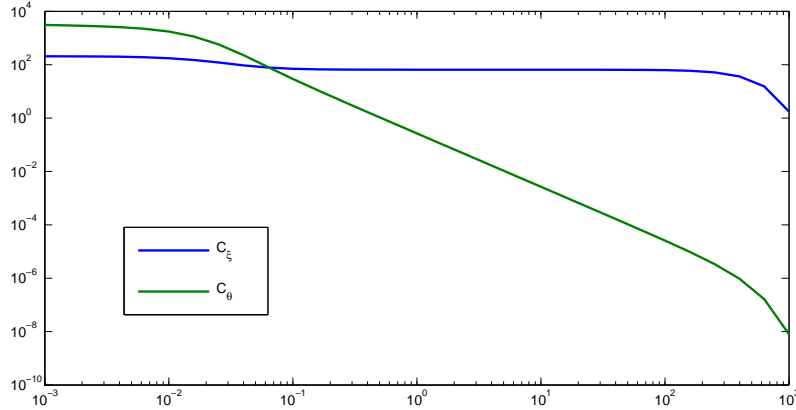
Figure 3.4: Maximum of the perturbations in free-volume and temperature for varying $\tilde{\omega}$. Applied Strain rate is fixed at $\dot{\gamma}_0 t = 2 \cdot 10^{-6}$.

3.3 Simple Shear Model for Machining Experiments

The work of [5] incorporates free-volume dynamics into an altered homogeneous simple shearing model formulated in [12]. This model approximates the local dynamics (usually called the 'Primary Shear Zone') of machining experiments. In such experiments, if the machining depth is too large, a Hopf bifurcation occurs, causing a transition from continuous to discontinuous chip formation. The altered simple shear model is as follows

$$\dot{\gamma}^p = f(\theta, \tau, \xi) \tag{3.9}$$

$$\dot{\xi} = \eta(\xi_0 - \xi) + g(\theta, \tau, \xi) \tag{3.10}$$

$$\dot{\theta} = \upsilon(1 - \theta) + \beta\tau\dot{\gamma}^p \tag{3.11}$$

$$\dot{\tau} = \Lambda(\dot{\gamma} - \dot{\gamma}^p) \tag{3.12}$$

where ξ_0 is the initial free-volume, υ is a heat flow coefficient, η is a free-volume flow coefficient, Λ is an apparent shear modulus which incorporates the machining depth, and all other variables are the same as before. The first terms in the second and third equations model the diffusivities of free-volume and temperature in the material. This model gives a bridge between our analysis and actual experiments. See Figures 3.5a - 3.5d for numerical solutions.

4 Analysis of the Hadamard Instability and Method of Frozen Coefficients

The method of frozen coefficients looks at the autonomous system obtained by fixing an initial time t_0 and computing the eigenvalues of the now time-independent coefficient matrix $A(t_0)$ to determine the asymptotic stability of the corresponding solution. If the eigenvalues have negative real parts, then the solution to the frozen system is asymptotically stable. When the autonomous
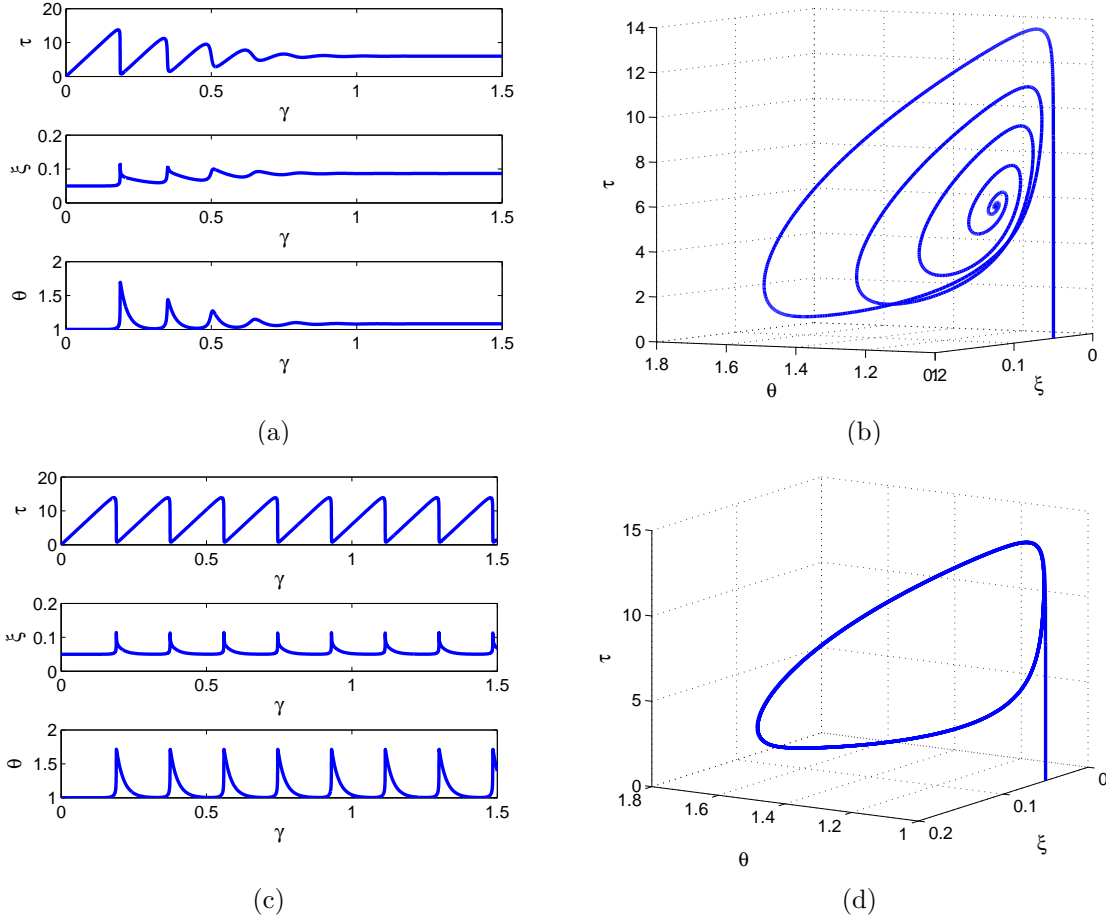
9

Figure 3.5: Solutions of machining model for various parameters **(a)+(b)** $\upsilon = 0.4$ & $\eta = 0.1$, **(c)+(d)** $\upsilon = 0.4$ & $\eta = 0.4$. Bifurcation point occurs $\eta \sim 0.132$.

system is Hadamard stable for all values t_0, we expect the stability of the frozen system to coincide with the stability of the non-autonomous system.

For a fixed time t_0, the non-zero eigenvalues of the coefficient matrix $A(t_0)$ are simply the eigenvalues of the 2×2 matrix

$$
\begin{pmatrix}
\frac{\partial f}{\partial \xi} & \frac{\partial f}{\partial \theta} \\[2mm]
\frac{\partial g}{\partial \xi} & \frac{\partial g}{\partial \theta}
\end{pmatrix}
\tag{4.1}
$$

Our simulations show that for k sufficiently large, the eigenvalues of (4.1) are negative for all fixed t_0. This suggests that the amplitudes of high-frequency perturbations do not grow without bound. As a result, we avoid the problem of Hadamard instability and conclude that the stability of the non-autonomous system follows from the stability observed in the frozen systems as shown in Figure 4.1. These results coincide with the observed behavior of the dimensionless PDE system.

Although the method of frozen coefficients can be used to examine asymptotic stability of the perturbed solutions, the results of such analysis are not always valid for the non-autonomous system.
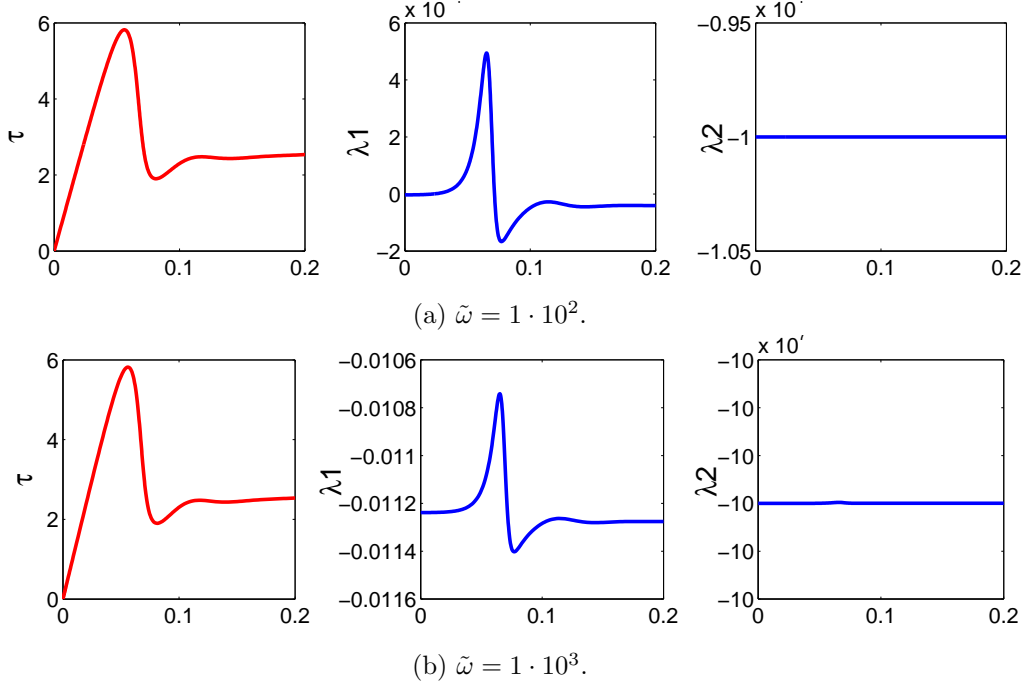
Figure 4.1: The stress-strain curve is plotted in red. The blue curves show the behavior of the real part of the eigenvalues of matrix $A(t)$ as $\tilde{\omega}$ increases.

5 Analysis of PDE's Dynamics

5.1 Initial and Boundary Conditions

The model (2.3) is at rest initially with no stress. The initial free-volume concentration and temperature are uniform, representing the perfect material. In subsequent simulations, a periodic perturbation will be added to the initial condition values in both free-volume concentration and temperature.

$$
\begin{aligned}
\xi|_{t=0} &= 0.05 \\
\theta|_{t=0} &= 1.
\end{aligned}
$$

In equations (2.3), the energy equation and the free-volume equation are reaction-diffusion equations. Here no flux boundary conditions are imposed as suggested by [6] to mimic the physical situation. The model is driven by a constant rate of strain on the boundary:

$$
\begin{aligned}
\frac{\partial \xi}{\partial y}\Big|_{y=0} &= \frac{\partial \xi}{\partial y}\Big|_{y=L} = 0 \\
\frac{\partial \theta}{\partial y}\Big|_{y=0} &= \frac{\partial \theta}{\partial y}\Big|_{y=L} = 0 \\
\gamma|_{y=0} &= \gamma|_{y=L} = \dot{\gamma}_0 t.
\end{aligned}
$$

5.2 Numerical method

Due to time restriction. we choose a simple numerical scheme. Being a reaction-diffusion equation, fast transients and sharp spikes may appear. For these a more sophisticated method will be needed. In the simple shear model, the reaction terms are dealt with explicitly, and the diffusion terms are dealt implicitly using Crank-Nicolson method to eliminate the restrictive CFL condition. Our scheme is as follows,

$$
\begin{aligned}
\gamma_{n+1}^P &= \gamma_n^P + \Delta t f(\xi_n, \theta_n, \tau_n) \\
\theta_{n+1} &= (I - K\frac{A}{2})^{-1}[(I + K\frac{A}{2})\theta_n + \beta_3 \tau_n \frac{\gamma_{n+1}^P - \gamma_n^P}{\Delta t}] \\
\xi_{n+1} &= (I - \beta_4 K\frac{A}{2})^{-1}[(I + \beta_4 K\frac{A}{2})\xi_n + g(\xi_n, \theta_n, \tau_n)] \\
\tau_{n+1} &= \mu(\dot{\gamma}_0 t_{n+1} - \gamma_{n+1}^P)\big|_{y=L}
\end{aligned}
$$

with $K = \Delta t / \Delta x^2$ and the second order center differentiation matrix with homogeneous Neumann boundary conditions

$$
A = \begin{pmatrix}
1 & -1 & & & \\
-1 & 2 & -1 & & \\
& \ddots & \ddots & \ddots & \\
& & \ddots & \ddots & -1 \\
& & & -1 & 1
\end{pmatrix}
$$

Moreover, to accelerate the simulation and better resolve the fast transition in time, we implement an adaptive time stepping scheme. The time steps are controlled the by the change in the free-volume and the temperature between steps.

5.3 Comparison with ODEs

We first check that the spatially homogeneous PDE solutions agree with the ODE solutions, as expected, in Figure 5.1.

To study and validate our linear perturbation analysis, small sinusoidal perturbations are added to both the free-volume concentration and temperature initial conditions:

$$
\xi|_0 = \xi_h + \delta \cos(wx)
$$

$$
\theta|_0 = \theta_h + \delta \cos(wx).
$$

In [3], Gao et al. show that there is a critical curve for wavenumber as a function of loading strain rate which delineates thermal instability, see Figure 3.2. In order to analyze this curve we choose two perturbations, one below and one above the critical line M_i. The amplitude of the perturbation is chosen to be small enough in order to match the linear perturbation analysis. In both Figures 5.2a and 5.2b, we see good agreement between the PDE solution and the linear perturbation results.
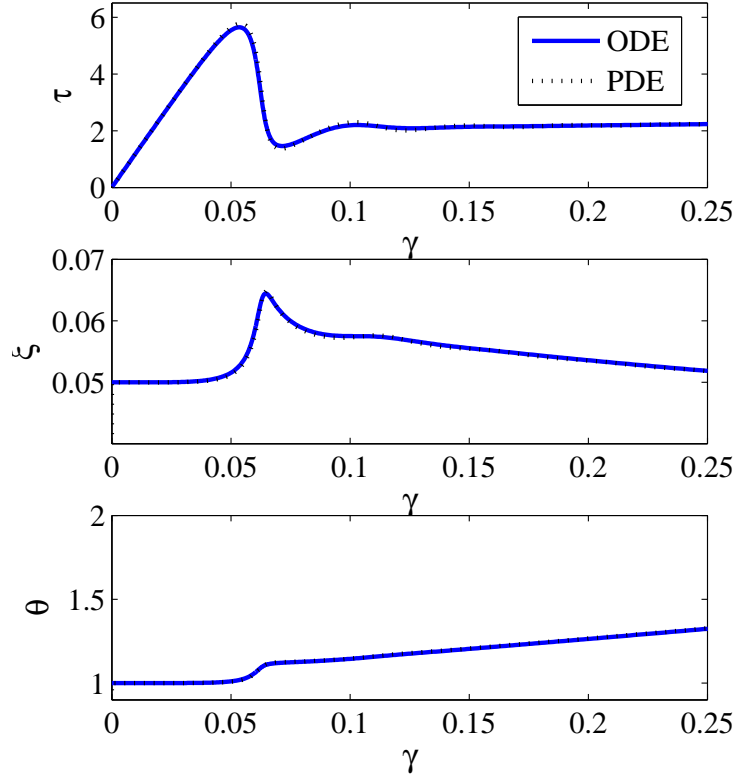
Figure 5.1: Comparison of spatially homogeneous solution from PDEs and ODEs.

This indicates that the perturbation is regular, and hence the ODEs are a good approximation of the PDE dynamics, at least for small perturbations. However, for such small amplitudes, we can barely see any sharp shear band formation. Furthermore, if the long time behavior is reliable, the results tell us the shear band (perturbation) will eventually disappear and only homogeneous solutions could be observed as we can see from Figures 3.3 and 5.3.

If a gaussian perturbation of sufficiently large amplitude is added to the initial free-volume concentration, we can see an exponential strain growth in the position where the perturbation is largest. See Figure 5.4. In this case, the time step length will decrease and the model cannot move forward. The sharp spike indicates the shear band is forming. Outside the shear band, the plastic strain increases slowly. However, there is not enough evidence to say that this is a finite time blowup.

For smaller gaussian perturbations, the amplitude of the perturbation starts to decay after the stress-strain curve turns down. This shows the same trend as in the linear perturbation analysis above. See Figure 5.5.

5.4 Stability Criteria

Figure 5.6b studies stability of perturbations. Here the color depicts the norm of fluctuation in temperature at a given strain rate and wavenumber. Similarly, Figure 5.6a give a similar plot for fluctuations in strain. It can be seen that both fluctuations get bigger as the strain rate becomes
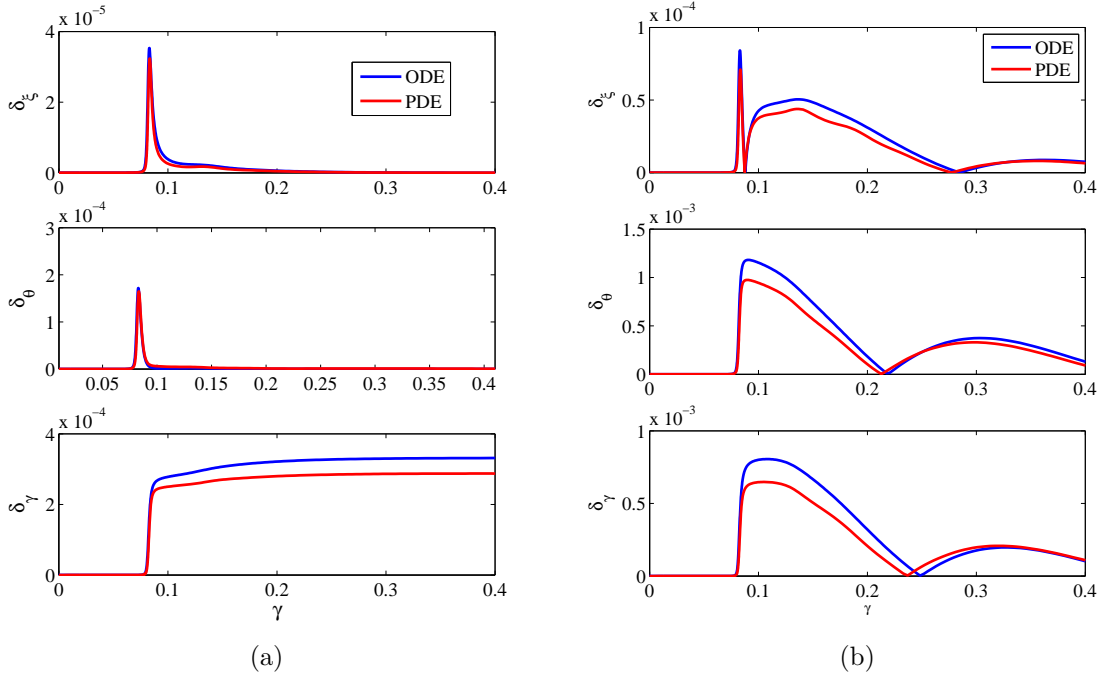
Figure 5.2: Perturbation in ξ and θ of magnitude $5 \cdot 10^{-8}$ and wave number .01 for **(a)** and .1 for **(b)**.

higher for small wavenumbers. Though the trend is similar, there is not a clear boundary on the amplitude of the perturbations in temperature or strain, unlike the critical line given from [3] or [4].

5.5 Strain Rate Hardening

If we vary the strain rate, we can see the maximum of stress is bigger for faster strain rate, while there is no obvious change when wavenumbers vary. Clifton denoted this as stain-rate sensitivity [1]. Numerics show that the strain rate hardening exhibits a logarithmic growth. One may draw the analogy with viscous fluids when a large velocity gradient causes large viscous force. However, in the dimensionless model, change in strain rate is equivalent to a rescaling of time; hence, faster movement may bring back the inertial force. In this case, stress will not be spatially homogeneous.

6 Conclusions

In this work we have performed an analysis of the simple shearing model for strain localization in bulk metallic glasses. In step with much of the previous literature, we performed a linear stability analysis, obtaining a system of non-autonomous linear ODEs which describe the evolution of periodic perturbations of the homogenous solution. To our knowledge, our study is the first work which has actually simulated these non-autonomous equations. From these simulations we have found that free-volume, and not temperature, dominates the growth of instabilities in most
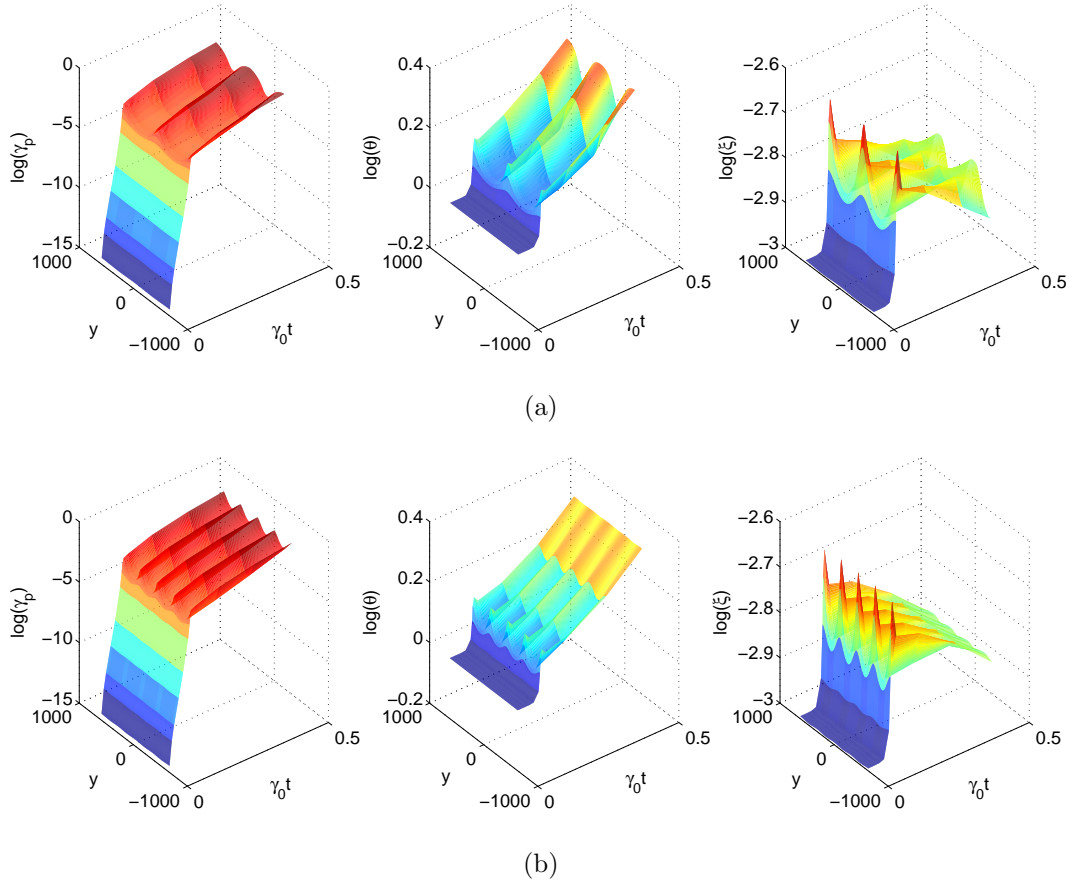
Figure 5.3: The evolution for different wavenumbers, **(a)** .01 and **(b)** .1

regimes, disagreeing with the work of [3] and agreeing with the frozen coefficient analyses of [6] and the experimental results of [10].

We also use simulations of the full 1-D constitutive PDE model to confirm our linear (ODE) results. In particular, we find that the nonlinear dynamics are well-approximated by the linearized system for small perturbation sizes and surprisingly long time scales. Additionally, we find for long times all perturbations decay. As shear bands usually do not decay in experiments, this suggests that the underlying model is not accurate in the long time regime. Hence, we postulate that the simple shear model should only be implemented as an *onset* equation and a more sophisticated physical model be used once the material begins to localize into one or more shear bands.

There are still many open avenues for mathematical analysis in this area. To our knowledge the transient and asymptotic behavior of the non-autonomous equations have yet to be subjected to a full theoretical study. Additionally, a mathematically rigorous PDE stability analysis has not yet been performed. Such an analysis would shed light on how perturbations evolve and possibly lead to wavenumber predictions in machining and indentation experiments. Finally, a study (numerical and theoretical) of these equations in higher dimensional spatial domains is needed to compare to experiment and molecular dynamics simulations.
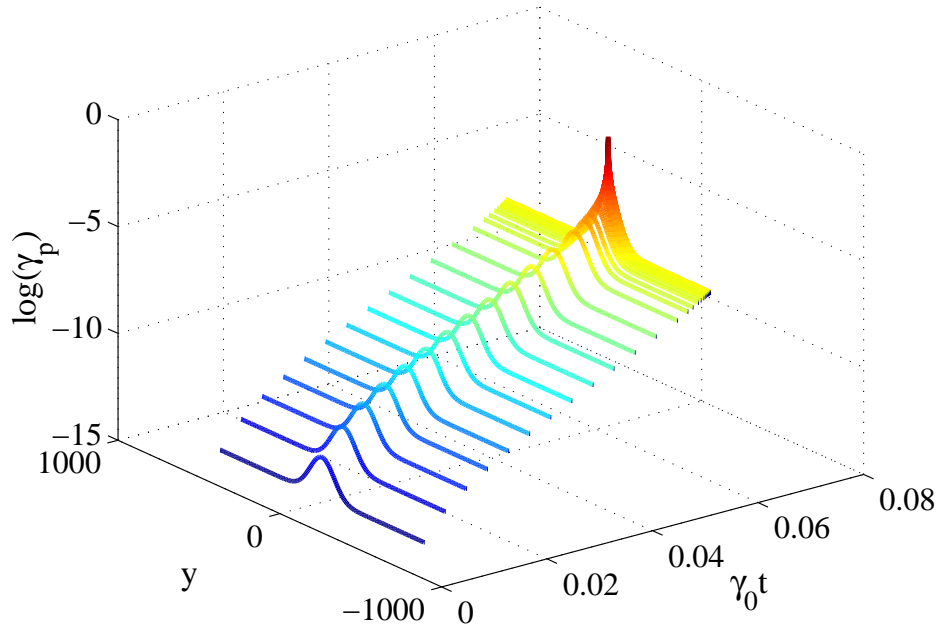
Figure 5.4: Gaussian perturbation generates shear band. PDE code parameters: $\dot{\gamma}_0 t = 2 \cdot 10^{-5}$ and relative height .1
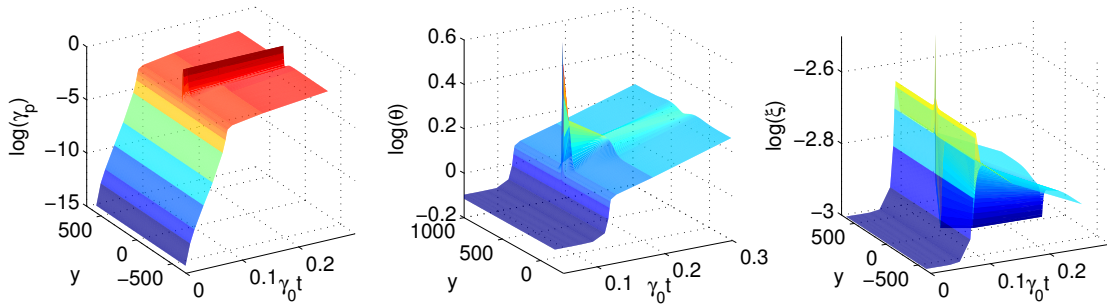

Figure 5.5: Small amplitude perturbation vanishes in long time with width $= 1$, and amplitude $= 3 \cdot 10^{-4}$.

References

[1] R.J. Clifton, J. Duffy, K.A. Hartley, and T.G. Shawki, On critical conditions for shear band formation at high strain rates, *Scripta Metallurgica 18* (1984) 443-448.

[2] L.H. Dai, M. Yan, L.F. Liu, and Y.L. Bai, Adiabatic shear banding instability in bulk metallic glasses, *Applied Physics Letters 87* 141916 (2005).

[3] Y. F. Gao, B. Yang, and T.G. Nieh, Thermomechanical instability analysis of inhomogeneous deformation in amorphous alloys, *Acta Materialia 55* (2007) 2319-2327.

[4] R. Huang, Z. Suo, J.H. Prevost, and W.D. Nix, Inhomogeneous deformation in metallic glasses, *Journal of the Mechanics and Physics of Solids 50* (2002) 1011-1027.
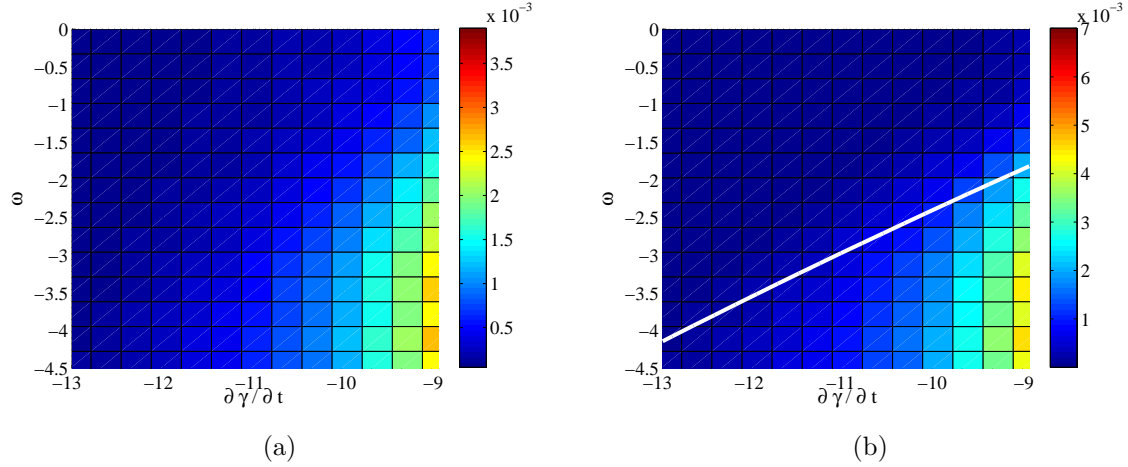
Figure 5.6: Fluctuations in strain **(a)** and temperature **(b)**. White curve denotes stability curve in [3].
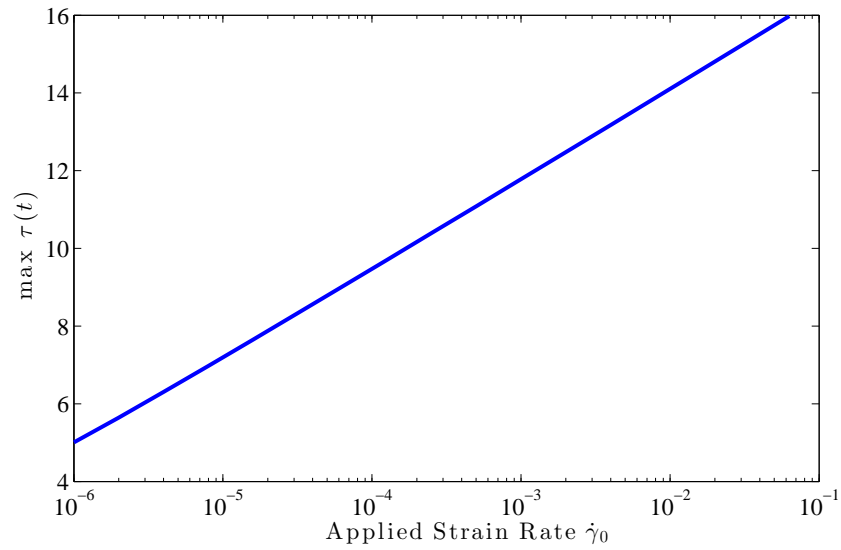

Figure 5.7: Maximum of stress increases logarithmic with loading strain rate.

[5] M.Q. Jiang, L.H. Dai, Formation mechanism of lamellar chips during machining of bulk metallic glass, *Acta Materialia 57* (2009) 2730-2738.

[6] M.Q. Jiang, L.H. Dai, On the origin of shear banding instability in metallic glasses, *Journal of the Mechanics and Physics of Solids* (2009) 1267-1292.

[7] K. Josic & R. Rosenbaum, Unstable Solutions of Non-Autonomous Linear Differential Equations, *SIAM Review 50.*3 (2008) 570-84.

[8] D.D. Joseph & J.C. Saut, Short-Wave Instabilities and Ill-Posed Initial-Value Problems, *Theoretical Computational Fluid Dynamics 1* (1990) 191-227.

[9] A.S. Argon, Plastic Deformation in Metallic Glasses, *Acta Metallurgica 27* (1978) 47-58.

[10] J.J. Lewandowski & A.L. Greer, Temperature Rise at Shear Bands in Metallic Glasses, *Nature Materials 5* (2006) 15-8.

[11] F. Spaepen, Must Shear Bands be Hot?, *Nature Materials 5* (2006) 7-8.

[12] T.J. Burns, & M.A. Davies, Nonlinear Dynamics Model for Chip Segmentation in Machining, *Physical Review Letters 79*(3) 447-50.

[13] T.W. Wright, The Physics and Mathematics of Adiabatic Shear Bands, *Cambridge University Press*, 2002.

[14] "Mechanical Behavior of Bulk Metallic Glasses", *R.H. Dauskardt Research Group,* Web: http://dauskardt.stanford.edu/kathy_flores/BMG/bmg.html.

A List of Parameters

Parameter	Description	Values from [3]
τ	Shear Stress	
γ	Total Strain	
θ	Temperature	$\theta/T_0 = 1$
ξ	Free-Volume	Scaled $\xi/\alpha v^* = 0.05$
α	Geometric Factor	0.15
ν	Poisson's Ratio	0.3
v	Atomic Vibration	$1 \cdot 10^{13} \mathrm{s}^{-1}$
v^*	Critical Volume (Hard-Sphere Atom)	$2 \cdot 10^{-29} \mathrm{m}^3$
ΔG^m	Activation Energy	0.4762 (0.2 - 0.5) eV
Ω	Atomic Volume	$2 \cdot 10^{-29} \mathrm{m}^3$
n_D	# Atomic Jumps needed to fill ξ equal to $v*$	Ranges from 3- 10
μ	Elastic Modulus	$\mu/\tau_0 = 120$
μ^*	Effective Elastic Modulus	$\frac{2}{3}\mu\frac{1+\nu}{1-\nu}$
τ_0	Scaling Factor for τ	$2k_B T_0/\Omega = 414$ MPa
k_B	Bolzmann's Constant	$8.6173324 \cdot 10^{-5}$ eV/K
ρ	Material Density	6810 kg/m^3
C_P	Specific Heat of Material	330 J/(kgK)
k	Thermal Conductivity	20 W/(mK)
l	Characteristic ξ Diffusion Length	$0.1 \cdot 10^{-9}$m
$\tilde{k}$	Diffusivity of ξ	$\nu \cdot \exp(-\Delta G^m/k_b T_0) \cdot l^2$
t_0	Characteristic Time Scale	$1 \cdot 10^{-5}$ s
α_{TQ}	Phenomenological parameter	0.9
β_1	Dimensionless Parameter	$v^*/\Omega = 1$
β_2	Dimensionless Parameter	$\Delta G^m/k_B T_0$
β_3	Dimensionless Parameter	$\alpha_{TQ}\tau_0/\rho C_P T_0 = 0.553$
β_4	Dimentionless Parameter	$\tilde{k}\rho C_p/k = 1 \cdot 10^{-10}$
$t_0\dot{\gamma}_0$	Normalized strain rate	$2 \cdot 10^{-6}$
L	Heat Conduction length	$\sqrt{kt_0/\rho C_p} = 9.4\mu$m
T_g	Glass Transition Time	